ADVANCED MATERIALS
www.advmat.de

Coding Acoustic Metasurfaces

Boyang Xie, Kun Tang, Hua Cheng, Zhengyou Liu, Shuqi Chen,* and Jianguo Tian**

Conventional metamaterials, which are artificial structures and can be described as effective media with effective parameters in general,[1,2] have aroused a tremendous interest in the past decade. Both the electromagnetic and acoustic metamaterials have been developed, which, with the greatly extended parameter space to natural materials, have demonstrated lots of promising applications, including super- or hyper-imaging,[3,4] beam steering,[5,6] and cloaking.[7,8] Recently, there has been a considerable interest in metasurfaces, a new kind of planar metamaterials, which have a subwavelength dimension in thickness and a repeated phase variation from 0 to 2π on the surface. With the capability of implementing acoustic devices extremely compact, metasurfaces have exhibited practical prospect in wave manipulations. Since the first realization of the optical metasurfaces by Yu et al.,[9] there have been a lot of efforts to explore the fascinating phenomena relevant to metasurfaces for both the electromagnetic and the acoustic waves.[10–14] Numerous intriguing properties have been revealed, such as anomalous reflection and refraction,[9,15–21] wave bending,[22,23] wave focusing,[24,25] vetor fields,[26] and wave converting into surface wave polaritons.[27,28] The key physics behind these phenomena lie in the generalized Snell's law, established itself on the gradient-phase on metasurfaces. However, most of the metasurfaces only work at a single frequency.[16,17,19,23,25,28] From the practical viewpoint, a broadband metasurface is useful, but it is difficult to implement. Since the gradient phase on the metasurface is approximated by limited discretized elements (for example, eight elements carrying phase from 0 to 2π) in practice, obviously it is difficult to allow waves in a wide frequency range transmitting through all the elements with the same amplitudes and the required phases. Therefore, to get a broadband acoustic metasurface still remains challenging.

In addition to the conventional metamaterials and the metasurfaces aforementioned, another alternative of the metamaterials, termed the digital or coding metamaterials, has recently been developed for the flexibility in the electromagnetic wave control,[29–32] which combine only limited kinds (typically two) of building elements, called Boolean numbers or logical bits, to realize different complicated functions, including steering, bending, focusing, and randomly scattering of electromagnetic waves. The assembly of the elements is similar to the functional units in a computer system, built on a binary system of only two numbers, "0" and "1," standing for the "off" and "on" states, respectively. The simplest coding metamaterials contain only two kinds, i.e., the "0" and "1" of elements, which can be realized, for example, by engineering two structure units to give rise to the phases of "0" and "π."

Although coding metamaterials have received wide attention in the community of electromagnetic waves and optics, so far there is no counterpart for acoustic waves, i.e., the coding acoustic metamaterials or metasurfaces reported. Here we present for the first time the coding acoustic metasurfaces by using the coding sequences of designed Boolean elements and show that acoustic waves can be manipulated by the coding metasurfaces with great flexibility. Moreover, as acoustic waves in a wide frequency range transmit the two building elements with equal amplitude and "π" phase shift, our devices can work in a certain bandwidth. As examples, the acoustic waves radiation and focusing mediated by the coding metasurfaces, are demonstrated by both numerical simulations and experiments.

The first and the most important step toward a functional coding metasurface (or metamaterial in general) is the design of the coding elements, which are the basic building blocks of the whole metasurface. For the binary coding metasurfaces, the most intuitive requirement for the design of the coding elements, i.e., the bits "0" and "1," when acoustic waves transmit through the two elements, they should be with the same amplitudes but out of phase or with a phase shift of π. From this consideration, it can be noticed that the coding elements of "0" and "1" are nothing but the two specific elements in all the elements (eight ones for example) building conventional metasurfaces with gradient phase varying from 0 to 2π. However, since the binary coding metasurfaces only involve two elements instead of multiple elements as building the conventional metasurfaces, it is comparatively easier to make the two elements work consistently (say with nearly the same amplitude but out of phase) in a wider frequency range. Therefore, although it is difficult to achieve broadband conventional metasurfaces, it is possible to realize certain bandwidth in coding metasurfaces with only Boolean elements.

The two-element coding surface designed for airborne sound are depicted in **Figure 1**a, with bit "0" in Figure 1b and bit "1" in Figure 1c. As can be seen, the two elements are equally sized and have similar structures inside. Each of them consists of two solid plates (yellow colored for bit "0," and blue colored for bit "1") separated by a small gap, with the lower plate being uniform in thickness and the upper plate with six rectangular grooves. For each element, there are two narrow slits, opened

Dr. B. Xie, Prof. H. Cheng, Prof. S. Chen, Prof. J. Tian
The MOE Key Laboratory of Weak Light Nonlinear Photonics
School of Physics
TEDA Institute of Applied Physics
and the 2011 Project Collaborative Innovation Center for Biological Therapy
Nankai University
Tianjin 300071, China
E-mail: hcheng@nankai.edu.cn; schen@nankai.edu.cn; jjtian@nankai.edu.cn

Dr. K. Tang, Prof. Z. Liu
School of Physics and Technology and Institute for Advanced Studies
Wuhan University
Wuhan 430072, China

DOI: 10.1002/adma.201603507

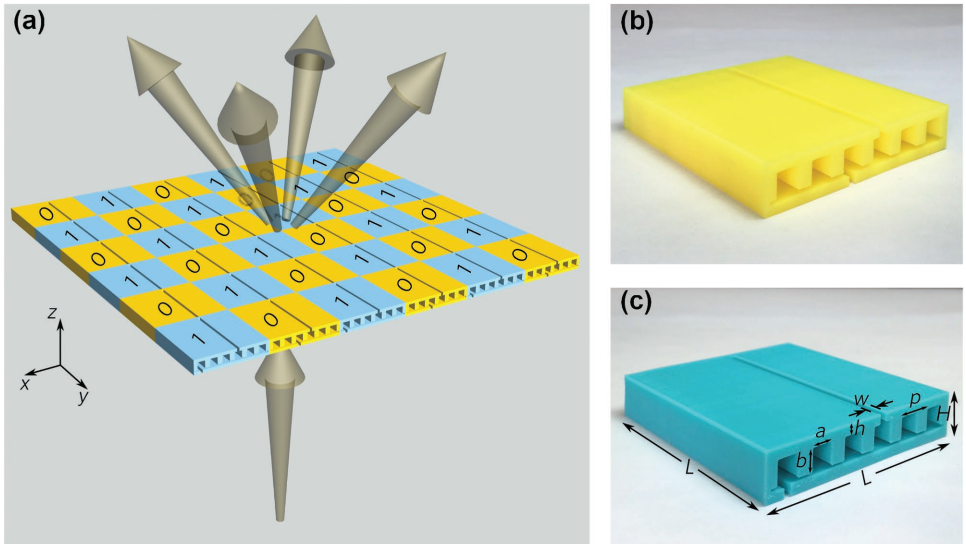

Figure 1. a) The schematic of the planar coding metasurface composed of squared coding element "0" and "1." Translucent arrows indicate the incident and transmitted waves. Photograph of the fabricated b) "0" and c) "1" coding elements.

on the upper plate and the lower plate, respectively. The slit on the lower plate is the entrance while the slit on the upper plate is the exit for acoustic waves incident upon the unit from below. Actually, if examining the structure, the only difference found between bits "0" and "1" lie in the position of the opening on the lower plate: for bit "0," the opening locates at $\Delta x = p$ to the opening on the upper plate, but for bit "1," the opening is at $\Delta x = 3p$ relatively, as the separation between the grooves is p. With the similar inner structure, it ensures that the two elements share the same resonant mode inside, so that the waves transmitting through bit "0" and bit "1" can have nearly the same amplitude. Meanwhile, with the exit slits opened in different position on the lower plate, the acoustic waves, entered from below with the same phase, can have different phases when exiting from bit "0" and "1" (The theoretical analysis is shown in Figure S1 (Supporting Information). The optional diversity of bits "0" and "1" is shown in Figures S2 and S3, and Table S1, Supporting Information). With a proper design as that shown in Figure 1, a phase difference of π has been obtained, as will depicted after. Taking the length (along x axis) of the two elements to be L, all the geometric parameters in the designs, as indicated in Figure 1, can all be detailed here, including the total thickness of the elements, $H = 6L/31$ ($\approx 0.61\ \lambda$), the thickness of the plates, $h = 5L/124$, the width of the narrow slits, $w = 1L/31$, the width and height of the rectangular grooves, $a = 2L/31$ and $b = 3L/31$, respectively, and the separation between the grooves, $p = 5L/31$. The narrow slit on the upper plate locates at position $18L/31$ (measured from the left end of the elements) for both bits "0" and "1," while that on the lower plate locates at $13L/31$ for bit "0," but at $3L/31$ for bit "1." We take L of 6.2 cm for all experiments in this paper.

To numerically calculate the amplitude and the phase of acoustic waves transmitting through bits "0" and "1," full-wave simulations are performed using the commercial software, COMSOL Multiphysics, based on the finite-element method. The material of coding elements is viewed as acoustically rigid, and the standard parameters used for air are sound speed $c_0 = 343$ m s^{-1} and mass density $\rho_0 = 1.2$ kg m^{-3}. We employ the periodic boundary condition, which corresponds to launching an acoustic plane waves normally onto the 2D array of bit "0" or bit "1." The result is shown in **Figure 2**. To our satisfaction, we observe that the amplitudes of the transmitted waves for bit "0" and bit "1" remain coincided, while maintaining the phase difference of π (Figure 2b) in the whole frequency range. The phases of the acoustic waves transmitting through the arrays of bit "0" and bit "1" are measured through 1D coding metasurface of 000000... and 111111..., with a microphone put in the center of the receiving area. The experimental details can be found in the description of the Experimental Section. The results, as given in Figure 1b, show that a phase shift around π remains for the two samples within a wide frequency range, which validates the design of the coding bits. The amplitudes exhibit a peak at wavelength $1.23L$, corresponding to the excitation of the resonant mode inside bits "0" or "1." Although the transmission is low away from the resonance, the phase difference remains π broadly. Therefore, the coding elements, and expectedly the coding metasurface built from the coding elements, can work in a certain bandwidth, overcoming the weakness of the conventional metasurfaces working at a single frequency. That may be more useful in practice. Unlike conventional acoustic metasurfaces with structural units building on the mechanism of Fabry–Parot resonance, our design of the coding bits relies on the excitation of the local modes within the space between the nearest bumps inside the structures, which can be described with the equivalent inductance and capacitance circuit resonance. The local modes, when excited by the incident waves, give rise to the transmission peaks in the spectra. Figure 2c–f gives the velocity field distributions inside bit "0" and bit "1" at the resonant frequency, it clearly shows that, for bit "0," the wave leaving from the exit slit is out of phase with the wave entering the entrance slit (Figure 2e), while

Adv. Mater. 2016,
DOI: 10.1002/adma.201603507

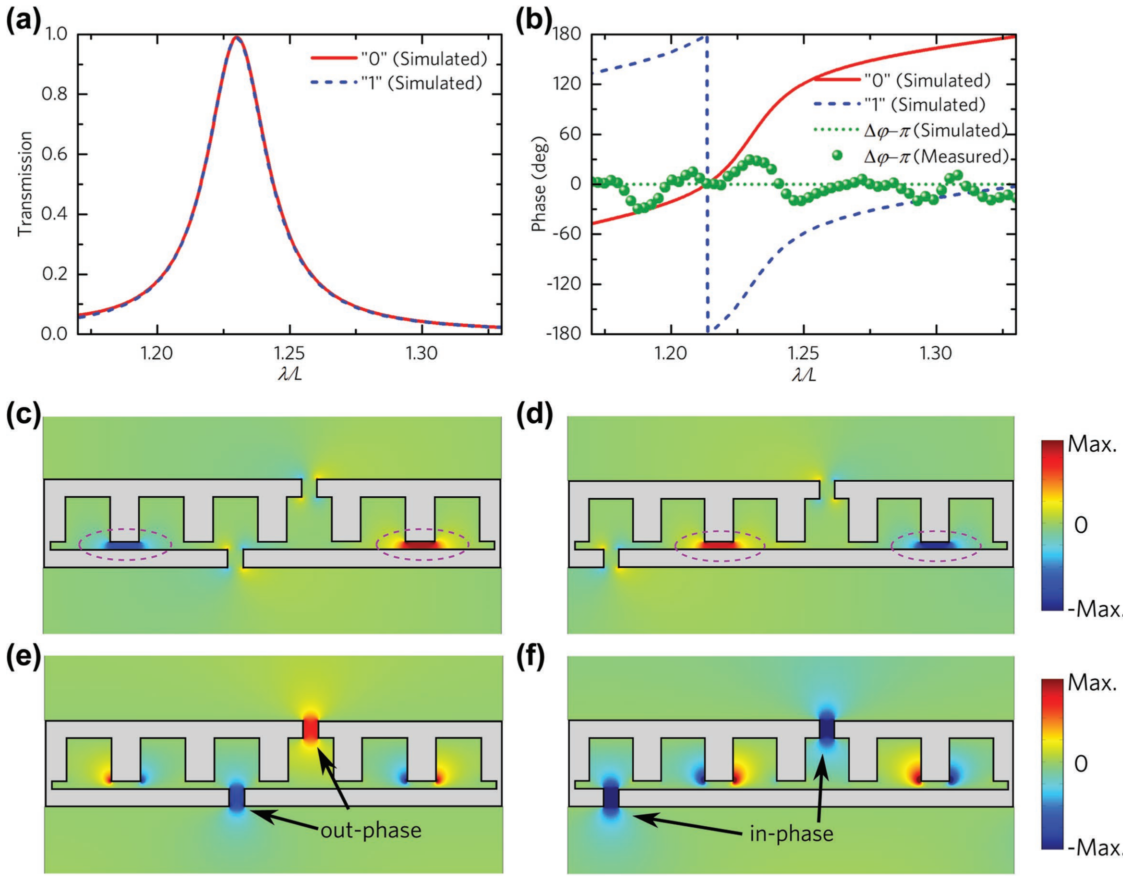

Figure 2. a) Transmission amplitude and b) phase of acoustic waves transmitting through the coding elements of "0" and "1." Temporal velocity fields of c,d) v_x and e,f) v_y in coding elements c,e) "0" and d,f) "1" at the resonant wavelength of 1.23L, respectively.

for bit "1," the waves are in phase (Figure 2f). As can also be noticed that, there are strong horizontal mass vibrations in the narrow gaps between the upper plate and the bumps of the lower plate (as indicated by the circles, in Figure 2c,d), signifying the occurrence of the resonance. Apparently, the local resonance is formed by the two-cavity resonant structure. The phase retardation through the two-cavities resonant structure is definitely π because the wave is coupled into the eigenmode corresponding to the point $k_x p/2\pi = 0.25$ in the first dispersion band. Here we use slit cavities to couple the wave in/out of the local resonance. Two slit cavities are directly connected for coding element "0" and connected to the left and right ends of a two-cavity resonant structure for coding element "1." Thus, the phase difference between the coding elements "0" and "1" is π. The details are shown in Figure S1 (Supporting Information). The intrinsic nature of the local resonance in our design and previous works is not exactly the same. The local resonances of our design are coupled with a particular mode supported by two linked cavities, which ensure the exact π phase difference and the same transmission, intrinsically making the structure more reliable in coding. Although some previous acoustic metamaterials represent much finer phase profiles and some works in broadband,[16,18] many of them suffer from the variant phase gradients with frequency, which may be not appropriate for coding applications. The phase difference does not change with frequency within a certain frequency band, which is the unique advantage of our designed device in coding. Compared with most of the metasurfaces, our designs of "0" and "1" share the similar shape and size except the location of the open slits, which not only provides great feasibility in practice but also has highly potentiality to realize active control between "0" and "1." The active control may be achieved by electrically switching on and off of the slits. We believe that the "coding" concept has its significance and is fundamental to realize further applications as active modulation. Moreover, based on the same mechanism, the much compact four-cavity structure can still generally meet the phase coding (see in Figures S2 and S3, Supporting Information). The lateral dimension may further be reduced by using multilayers, which contain fewer cavities in a layer.

Now we can use the two designed coding elements to program metasurfaces. We can suppose the square coding metasurface is composed of $m \times n$ elements by "0" or "1." The scattering phase of the mnth lattice is assumed to be $\varphi(m, n)$, which is either 0 or π. Under the normal incidence of the plane waves, the far-field function scattered by the metasurface is expressed as[30]

$$f(\theta,\varphi) = f_e(\theta,\varphi) \sum_{m=1}^{N}\sum_{n=1}^{N} \exp\left\{-i\left\{\varphi(m,n) + kL\sin\theta\left[\left(m-\frac{1}{2}\right)\cos\varphi + \left(n-\frac{1}{2}\right)\sin\varphi\right]\right\}\right\} \quad (1)$$

where θ and φ are the elevation and azimuth angles of an arbitrary direction, respectively, and $f_e(\theta, \varphi)$ is the pattern function of a lattice.

To show the effect of the coding metasurfaces, the wave beams are normally incident on the metasurfaces from below. For farfield simulations, each coding metasurface, lying in x-y plane, comprises of 6 × 6 elements and the incident beam has a size of 4 L × 4 L in cross section. For the limitation of experimental conditions (we used the B&K Type 4206 impendence tube, with diameter of 10 cm, as the plane wave sound source), only 2 × 2 elements are fabricated. Although the farfield radiating pattern of 2 × 2 elements is not exactly the same with that of 6 × 6 elements, e.g., the 6 × 6 sample shows better directivity, the elevation and azimuth angles of the main radiating branches for both cases are the same, which show the main features of the radiating branches. The results for the frequency of 4500 Hz are shown in **Figure 3**, with Figure 3a–d giving the simulated far field in the manner of angular distributions and Figure 3e–l giving the simulated and the corresponding experimental field amplitude distributions in x-y plane with 6.2 cm above the metasurfaces. Obviously, the simplest coding metasurface is the all "0" or all "1" metasurface, consisting of a 2D array of purely bits "0," or purely bits "1." The general formula of Equation (1) can be simplified as

$$\left|f_1(\theta,\varphi)\right| = C_1\left|\cos\psi_1 + \cos\psi_2\right| = 2C_1\left|\cos\frac{\psi_1+\psi_2}{2}\cos\frac{\psi_1-\psi_2}{2}\right| \tag{2}$$

where $\psi_1 = kL(\sin\theta\cos\varphi + \sin\theta\sin\varphi)/2$, $\psi_2 = kL(-\sin\theta\cos\varphi + \sin\theta\sin\varphi)/2$. To obtain the maximum scattering, the absolute values of the sinusoidal functions should be one, i.e., $|\cos[(\psi_1+\psi_2)/2]| = 1$, $|\cos[(\psi_1-\psi_2)/2]| = 1$. $\theta_1 = 0$ can be easily obtained. Thus, the main scattering beam will be transmitted along the incident direction. The farfield and the field amplitude in the x-y plane distributions also tell that the beam exiting from the metasurface remains its propagation along z-axis, without scattering into other directions (Figure 3a,e,i). However, if the metasurfaces are coded as 010101.../010101... in Figure 3b (01/01 in Figure 3f,j), 101010.../010101... in Figure 3c (10/01 in Figure 3g,k), or 01/00 in Figure 3h,l, Equation (1) can be also simplified, respectively, as

$$\left|f_2(\theta,\varphi)\right| = C_2\left|\sin\psi_1 + \sin\psi_2\right| = 2C_2\left|\sin\frac{\psi_1+\psi_2}{2}\cos\frac{\psi_1-\psi_2}{2}\right| \tag{3}$$

$$\left|f_3(\theta,\varphi)\right| = C_3\left|\cos\psi_1 - \cos\psi_2\right| = 2C_3\left|\sin\frac{\psi_1+\psi_2}{2}\sin\frac{\psi_1-\psi_2}{2}\right| \tag{4}$$

$$\left|f_4(\theta,\varphi)\right| = C_4\left|\cos\psi_2 - i\sin\psi_1\right| \tag{5}$$

We can also derive the extremal points as $\varphi_2 = 90°$ and 270°, and $\theta_2 = \arcsin[\lambda/(2L)]$ for 010101.../010101..., $\varphi_3 = 45°$, 135°, 225°, 315°, and $\theta_3 = \arcsin[\lambda/(\sqrt{2}L)]$ for 101010.../010101..., and more complex numerical solutions for 010101.../000000.... Then, the incident beam is scattered into two or four symmetrically radiating branches, or more complicated radiating branches. It is worth noting that, for the metasurfaces of all-"0" in Figure 3a (00/00 in Figure 3e,i), the all-"1" or the 010101.../010101... in Figure 3b (01/01 in Figure 3f,j), they are all actually translation-invariant along y direction, that is to say, the coding elements along y just join and can be viewed as an elongated element. Therefore, the three metasurfaces are essentially 1D, with the sequences 000000..., 111111..., and 010101..., composed of the elongated coding elements. In contrast, the coding 101010.../010101...in Figure 3c (10/01 in Figure 3g,k) and 010101.../000000... in Figure 3d (01/00 in Figure 3h,l) are truly 2D. The branching effects can be interpreted in terms of diffraction. For the coding 010101.../010101... in Figure 3b (01/01 in Figure 3f,j), the two branches are in fact the +1 and −1 diffraction orders of the 1D structure, appeared with the absence of the 0 diffraction order because of the destructive interference from bits "0" and "1." Similarly, the four branches for the coding 101010.../010101... in Figure 3c (10/01 in Figure 3g,k) belong to the first diffraction order of the 2D periodic structure, with the zero order absent. The forward scatterings are canceled because of the phase difference of π from the different scattering bits. However, there are both zero and first diffraction orders of the 2D periodic structure of coding 010101.../000000... in Figure 3d (01/00 in Figure 3h,l). The branching effects allow the coding metasurfaces to serve as the antenna in applications. Naturally, it can be expected that, if coding the bits more complicated, for example, coding randomly instead of periodically, more sophisticated control of acoustic waves should be able to achieve.

As aforementioned, the coding metasurfaces of all-"0," all-"1," and 010101.../010101 are essentially 1D. Thus the simulation and experiment can be significantly simplified. Our experiment for 1D coding metasurface is based on a planar waveguide system, which is easy to build up. The setup of experiment is schematically shown in **Figure 4**a, which gives the top view inside a planar waveguide. The samples in experiment are fabricated with an extension in y of 1.2 cm (see in Figure 4b). The sample is firmly sandwiched in the waveguide with the sample's wave-entrance faced, normally or obliquely, to the Gaussian beam. Slightly longer sample is used in the case of oblique orientation. The transmitted wave is measured in the blue-colored rectangular area. Figure 4b shows the photograph of the two coding elements "0" (above) and "1" (below), with cell size in x direction of L = 6.2 cm.

As an example, we demonstrate the wave branching by the metasurface coded in the sequence of 101010..., with varying frequency of the input waves, and varying orientation of the sample. In Figure 4c,d,e,f, we show the simulated and measured transmitted temporal field distributions (in an area of 104 cm × 66 cm, 2 cm above the sample) at frequencies of 4500 Hz, with wave normal (Figure 4c,d) and 10° oblique (Figure 4e,f) incidence, respectively. The transmitted temporal field and phase distributions for other frequencies are also measured and similar results are got (see in Figures S4 and S5, Supporting Information). As expected, in both the cases, and for all the frequencies, the incident wave is scattered into two refracted branches (indicated by the black arrows together with sequential equiphase planes). The experiment shows agreement with the simulations.

Adv. Mater. 2016,
DOI: 10.1002/adma.201603507

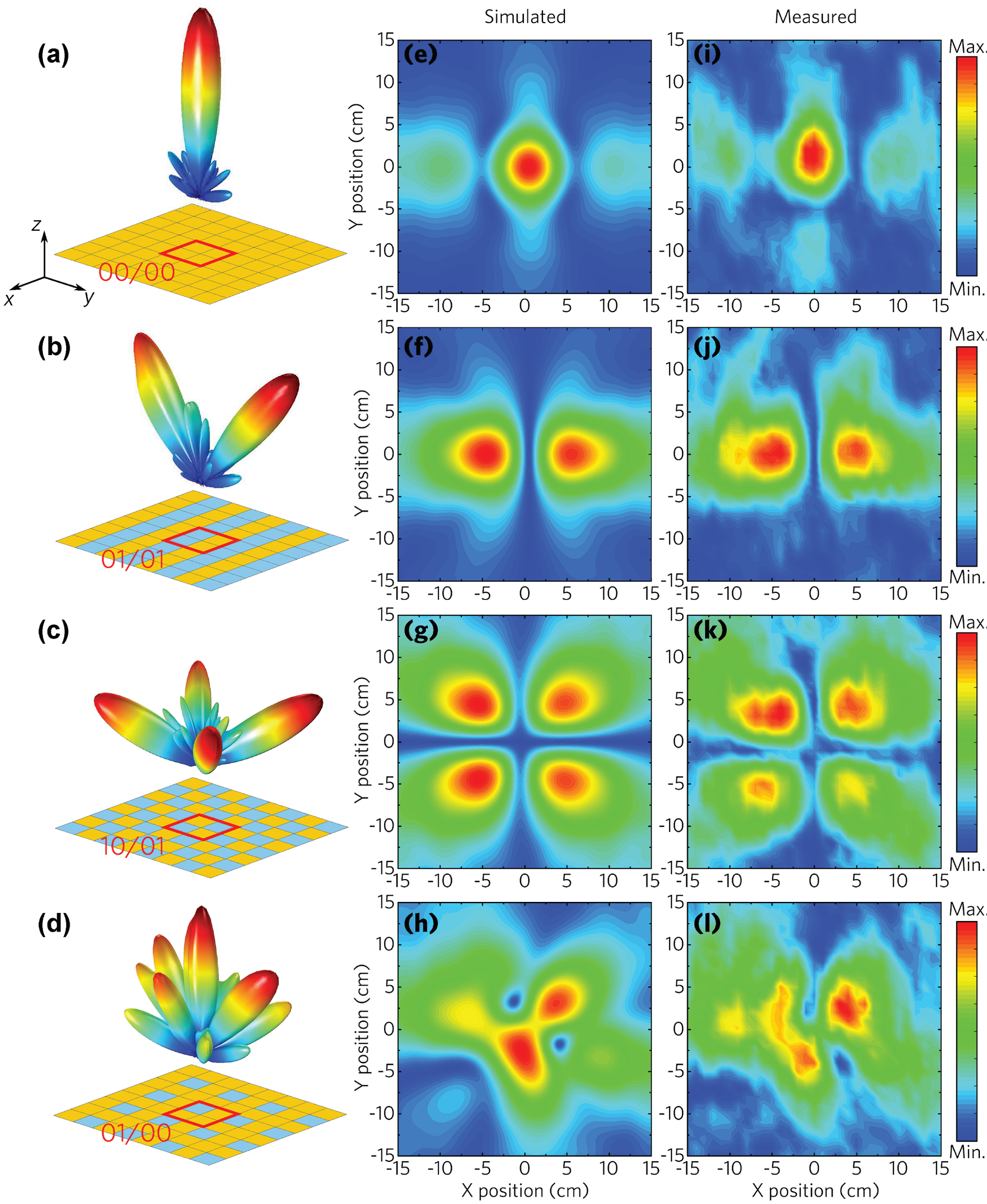

Figure 3. Simulated far field distributions of transmission through coding metasurfaces of a) 000000…/000000…, b) 010101…/010101…, c) 101010…/010101…, and d) 010101…/000000…. e–h) Simulated and i–l) experimental field amplitude distributions in *x-y* plane with 6.2 cm above the sample of transmission through simple coding of e,i) 00/00, f,j) 01/01, g,k) 01/10, h,l) 01/00.

Next, we demonstrate that a flat Fresnel zone plate can be programmed with the designed coding elements. **Figure 5**a shows schematically the structure of the device as well as the scheme to program it. Again, yellow denotes zones composed of bit "0," blue denotes zones composed of bit "1," and gray denotes acoustically rigid zones. To produce constructive interference at the focal point, the wave path difference between two successive zones should satisfy

$$l_{i+1} - l_i = \frac{\lambda}{2} \tag{6}$$

where $l_i = \sqrt{x_c^2 + r_i^2}$, ($i$ = 0, 1, 2, ...) is the wave path from zone i to the focal point, with x_c being the focal length and r_i the inner border radius of zone i, as labeled in Figure 4a. For zone 0, i.e., for the central zone, $r_0 = 0$. From Equation (6), we obtain

DOI: 10.1002/adma.201603507

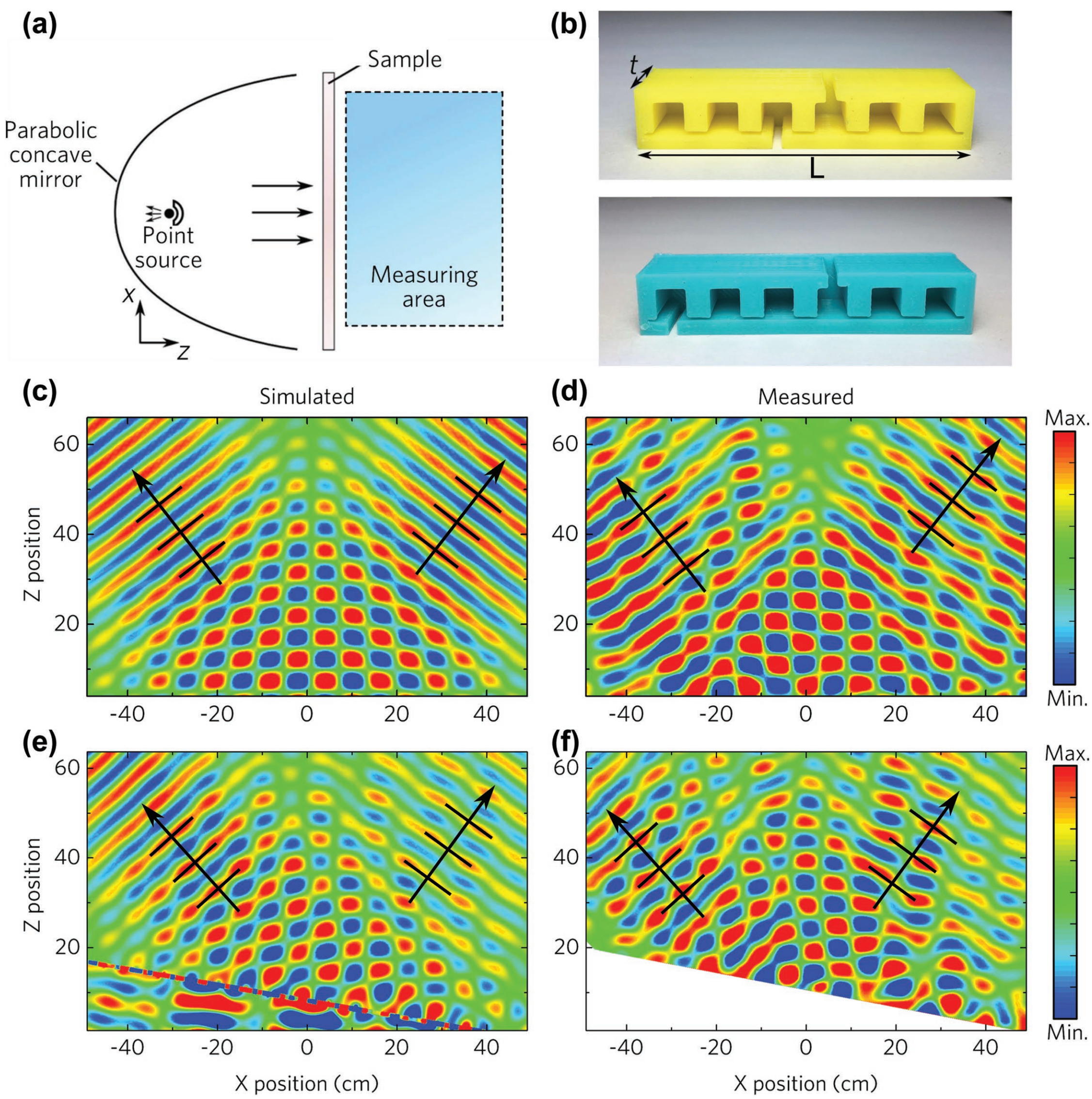

Figure 4. a) The schematic diagram of experimental system setup of the 1D coding metasurface. b) Photograph of the fabricated "0" and "1" coding elements. c,e) Numerical and d,f) experimental acoustic temporal field distribution of the transmitted wave for c,d) normal and e,f) 10° oblique incidence at 4500 Hz. The black lines and arrows indicate the wave fronts and propagating directions.

$$r_{i+1} = \sqrt{\left(\lambda/2 + \sqrt{x_c^2 + r_i^2}\right)^2 - x_c^2} \tag{7}$$

Below we exemplify a Fresnel lens designed with the focal length of x_c = 50 cm. From Equation (7), we get the zone parameters, r_1 = 19.9 cm, r_2 = 28.6 cm, r_3 = 35.7 cm, and r_4 = 41.9 cm for successive four zones. We choose five bits "1" at the center zone and arrays of alternate bit "0" and bit "1" for other zones with d_1 = 1.8 cm, d_4 = 0.8 cm, $d_2 = d_5$ = 2.5 cm, and $d_3 = d_6$ = 0.9 cm. Figure 5b,c shows the focusing of the incident plane waves by the lens at 4530 Hz achieved numerically and experimentally. As observed, with the zone numbers of 5, the Fresnel lens already demonstrates very excellent focusing performance. Especially, as shown in the insets of Figure 5c, this Fresnel lens also exhibits good performance for the focal plane as the full width at half maximum equals 4.6 cm, which is well confirmed by experiment. In contrast with the Fresnel lens based on the conventional metasurface (with zigzag structures inside)[25] focusing sound at a single frequency, the coding Fresnel lens here focuses wave in a certain bandwidth (This effect is shown in Figure S6, Supporting Information), although sound amplification may be lower at off-resonant frequency, due to the lower transmissions.

In conclusion, based on local resonant modes, we design binary structures, which can serve as the building elements or coding bits to compose variant functional metasurfaces working in a certain bandwidth. For bits "0" and "1," the transmitted wave has "π" phase shift but equal amplitude. The occurrence of phase difference is explained by the local resonance inside the bits. Metasurfaces coded with the coding bits which exhibit

Adv. Mater. 2016, DOI: 10.1002/adma.201603507

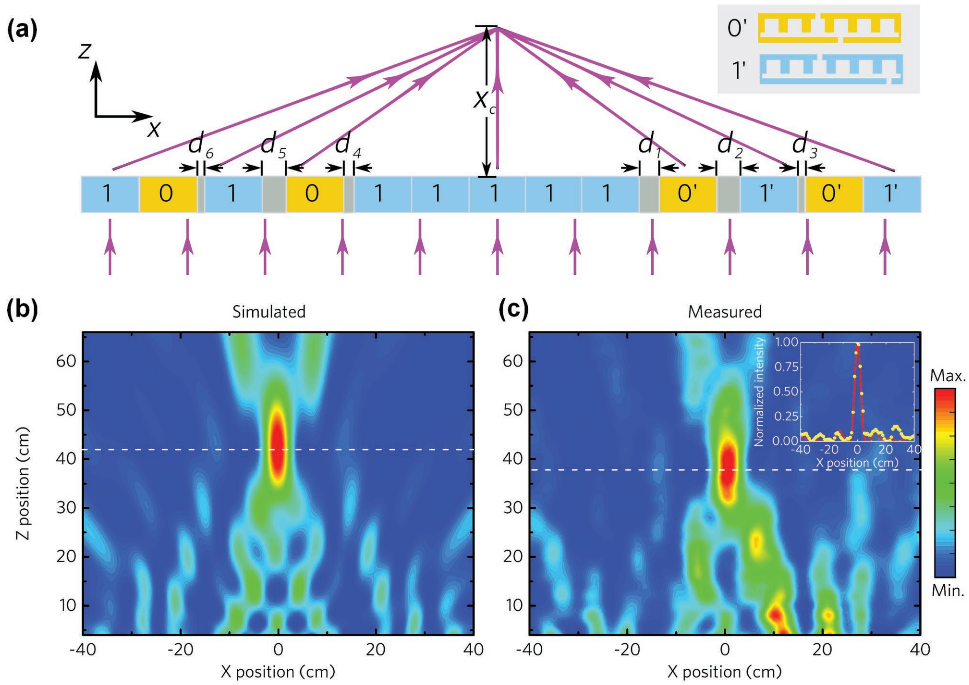

Figure 5. a) The schematic diagram for the design of a flat Fresnel lens ((0′ and 1′ are the mirror structure of 0 and 1). The b) numerical and c) experimental intensity profile for the focusing effect at frequency of 4530 Hz. Insets show the simulated (red line) and measured (yellow balls) intensities (normalized by the maximum values) distributed at the horizontal lines marked in (b) and (c).

wave branching effects, are demonstrated in simulations and in experiments. We also present the coding of Fresnel zone plate, which shows excellent focusing performance. With the concept of the acoustic coding metamaterials or metasurfaces, innovative acoustic devices may be developed and used in acoustic wave processing, digital lenses, diffusion cloaking and wave field modulations.

Experimental Section

Measurement Setup: The coding elements were fabricated of thermal plastics via fused deposition modeling with a commercial 3D printer. Measurements of the phases of acoustic waves transmitting through the coding elements shown in Figure 2b, 1D wave branching shown in Figure 4, and the focusing effect for flat Fresnel lens shown in Figure 5c were performed in our lab-made 2D acoustic waveguide with the height of t = 1.2 cm (≈0.16 λ). The whole waveguide was surrounded by the acoustical absorbent material, intending to reduce the reflection from the boundary. The sound produced by a B&K Type 4206 impendence tube was guided into the system by a tiny rubber pipe to mimic a point source, which lies at the foci of the parabolic solid wall on the left. The wave was reflected by the parabolic wall to mimic Gaussian beam (of width ≈40 cm, i.e., ≈5λ). The samples were placed in the center of the waveguide. To measure the transmitted acoustic field, two microphones (B&K 4187, 1/4-inch diameter) are used. One is fixed which serves as the phase reference, while the other one scans the field point by point (with a step of 2 cm). The acoustic signal is analyzed by a multianalyzer system (B&K Type 3560B), with which both the amplitude and phase of the wave are extracted. Similar measurements are used to acquire the 2D coding patterns shown in Figure 3, in which the coding metasurface is placed right on the impendence tube instead, and the transmitted wave is measured above the sample (scanned with a step of 1 cm).

Supporting Information

Supporting Information is available from the Wiley Online Library or from the author.

Acknowledgements

This work was supported by the National Key Research and Development Program of China (2016YFA0301102), the National Basic Research Program (973 Program) of China (2012CB921900), the Natural Science Foundation of China (11574163, 61378006, 11304163, and 11374233), the Program for New Century Excellent Talents in University (NCET-13-0294), and the 111 project (B07013).

Received: July 3, 2016
Revised: September 30, 2016
Published online:

[1] D. R. Smith, W. J. Padilla, D. C. Vier, S. C. Nemat-Nasser, S. Schultz, *Phys. Rev. Lett.* **2000**, *84*, 4184.
[2] Z. Liu, X. Zhang, Y. Mao, Y. Y. Zhu, Z. Yang, C. T. Chan, P. Sheng, *Science* **2000**, *289*, 1734.
[3] M. C. K. Wiltshire, J. B. Pendry, I. R. Young, D. J. Larkman, D. J. Gilderdale, J. V. Hajnal, *Science* **2001**, *291*, 849.
[4] J. Zhu, J. Christensen, J. Jung, L. Martin-Moreno, X. Yin, L. Fok, X. Zhang, F. J. Garcia-Vidal, *Nat. Phys.* **2010**, *7*, 52.
[5] R. B. Greegor, C. G. Parazzoli, J. A. Nielsen, M. A. Thompson, M. H. Tanielian, D. R. Smith, *Appl. Phys. Lett.* **2005**, *87*, 2005.
[6] S.-C. S. Lin, T. J. Huang, *J. Appl. Phys.* **2009**, *106*, 053529.
[7] T. Ergin, N. Stenger, P. Brenner, J. B. Pendry, M. Wegener, *Science* **2010**, *328*, 337.

[8] L. Zigoneanu, B.-I. Popa, S. A. Cummer, *Nat. Mater.* **2014**, *13*, 352.
[9] N. Yu, P. Genevet, M. A. Kats, F. Aieta, J.-P. Tetienne, F. Capasso, Z. Gaburro, *Science* **2011**, *334*, 333.
[10] D. Lin, P. Fan, E. Hasman, M. L. Brongersma, *Science* **2014**, *345*, 298.
[11] F. Aieta, M. A. Kats, P. Genevet, F. Capasso, *Science* **2015**, *347*, 1342.
[12] X. Ni, Z. J. Wong, M. Mrejen, Y. Wang, X. Zhang, *Science* **2015**, *349*, 1310.
[13] J. Zhu, Y. Chen, X. Zhu, F. J. Garcia-Vidal, X. Yin, W. Zhang, X. Zhang, *Sci. Rep.* **2013**, *3*, 1.
[14] Y. Cheng, C. Zhou, B. G. Yuan, D. J. Wu, Q. Wei, X. J. Liu, *Nat. Mater.* **2015**, *14*, 1013.
[15] F. Aieta, P. Genevet, N. Yu, M. A. Kats, Z. Gaburro, F. Capasso, *Nano Lett.* **2012**, *12*, 1702.
[16] Y. Xie, W. Wang, H. Chen, A. Konneker, B.-I. Popa, S. A. Cummer, *Nat. Commun.* **2014**, *5*, 5553.
[17] K. Tang, C. Qiu, M. Ke, J. Lu, Y. Ye, Z. Liu, *Sci. Rep.* **2014**, *4*, 6517.
[18] Y.-F. Zhu, X.-Y. Zou, R.-Q. Li, X. Jiang, J. Tu, B. Liang, J.-C. Cheng, *Sci. Rep.* **2015**, *5*, 10966.
[19] C. Ding, H. Chen, S. Zhai, S. Liu, X. Zhao, *J. Phys. D: Appl. Phys.* **2015**, *48*, 045303.
[20] Z. Liu, Z. Li, Z. Liu, J. Li, H. Cheng, P. Yu, W. Liu, C. Tang, C. Gu, J. Li, S. Chen, J. Tian, *Adv. Funct. Mater.* **2015**, *25*, 5428.
[21] H. Cheng, S. Chen, P. Yu, W. Liu, Z. Li, J. Li, B. Xie, J. Tian, *Adv. Opt. Mater.* **2015**, *3*, 1744.
[22] X. Ni, N. K. Emani, A. V. Kildishev, A. Boltasseva, V. M. Shalaev, *Science* **2012**, *335*, 427.
[23] Y. Li, X. Jiang, R. Li, B. Liang, X. Zou, L. Yin, J. Cheng, *Phys. Rev. Appl.* **2014**, *2*, 064002.
[24] F. Aieta, P. Genevet, M. A. Kats, N. Yu, R. Blanchard, Z. Gaburro, F. Capasso, *Nano Lett.* **2012**, *12*, 4932.
[25] K. Tang, C. Qiu, J. Lu, M. Ke, Z. Liu, *J. Appl. Phys.* **2015**, *117*, 024503.
[26] J. Li, S. Chen, H. Yang, J. Li, P. Yu, H. Cheng, C. Gu, H.-T. Chen, J. Tian, *Adv. Funct. Mater.* **2015**, *25*, 704.
[27] S. Sun, Q. He, S. Xiao, Q. Xu, X. Li, L. Zhou, *Nat. Mater.* **2012**, *11*, 426.
[28] Y. Li, B. Liang, Z. Gu, X. Zou, J. Cheng, *Sci. Rep.* **2013**, *3*, 2546.
[29] C. D. Giovampaola, N. Engheta, *Nat. Mater.* **2014**, *13*, 1115.
[30] T. J. Cui, M. Q. Qi, X. Wan, J. Zhao, Q. Cheng, *Light Sci. Appl.* **2014**, *3*, e218.
[31] L.-H. Gao, Q. Cheng, J. Yang, S.-J. Ma, J. Zhao, S. Liu, H.-B. Chen, Q. He, W.-X. Jiang, H.-F. Ma, Q.-Y. Wen, L.-J. Liang, B.-B. Jin, W.-W. Liu, L. Zhou, J.-Q. Yao, P.-H. Wu, T.-J. Cui, *Light Sci. Appl.* **2015**, *4*, e324.
[32] L. Liang, M. Qi, J. Yang, X. Shen, J. Zhai, W. Xu, B. Jin, W. Liu, Y. Feng, C. Zhang, H. Lu, H.-T. Chen, L. Kang, W. Xu, J. Chen, T. J. Cui, P. Wu, S. Liu, *Adv. Opt. Mater.* **2015**, *3*, 1374.

Adv. Mater. **2016**,
DOI: 10.1002/adma.201603507